

INVERSE MULTIVIEW II: MICROARCSECOND TRIGONOMETRIC PARALLAXES FOR SOUTHERN HEMISPHERE 6.7 GHz METHANOL MASERS G232.62+00.99 AND G323.74–00.26

L. J. HYLAND,¹ M. J. REID,² G. OROSZ,^{1,3} S. P. ELLINGSEN,¹ S. D. WESTON,⁴ J. KUMAR,¹ R. DODSON,⁵ M.J. ROIJA,^{6,5,7} W. J. HANKEY,¹ P. M. YATES-JONES,¹ T. NATUSCH,⁴ S. GULYAEV,⁴ K. M. MENTEN,⁸ AND A. BRUNTHALER⁸

¹*School of Natural Sciences, University of Tasmania, Private Bag 37, Hobart, Tasmania 7001, Australia*

²*Center for Astrophysics | Harvard & Smithsonian, Cambridge, MA 02138, USA*

³*Joint Institute for VLBI ERIC, Oude Hoogeveensedijk 4, 7991PD Dwingeloo, Netherlands*

⁴*Institute for Radio Astronomy and Space Research, Auckland University of Technology, 120 Mayoral Drive, Auckland 1010, New Zealand*

⁵*ICRAR, M468, The University of Western Australia, 35 Stirling Hwy, Crawley, Western Australia, 6009*

⁶*CSIRO Astronomy and Space Science, PO Box 1130, Bentley WA 6102, Australia*

⁷*Observatorio Astronómico Nacional (IGN), Alfonso XII, 3 y 5, 28014 Madrid, Spain*

⁸*Max-Planck-Institut fr Radioastronomie, Auf dem Hgel 69, D-53121 Bonn, Germany*

ABSTRACT

We present the first results from the Southern Hemisphere Parallax Interferometric Radio Astrometry Legacy Survey (S π RALS): 10 μ as-accurate parallaxes and proper motions for two southern hemisphere 6.7 GHz methanol masers obtained using the inverse MultiView calibration method. Using an array of radio telescopes in Australia and New Zealand, we measured the trigonometric parallax and proper motions for the masers associated with the star formation region G232.62+00.99 of $\pi = 0.610 \pm 0.011$ mas, $\mu_x = -2.266 \pm 0.021$ mas y^{−1} and $\mu_y = 2.249 \pm 0.049$ mas y^{−1}, which implies its distance to be $d = 1.637 \pm 0.029$ kpc. These measurements represent an improvement in accuracy by more than a factor of 3 over the previous measurements obtained through Very Long Baseline Array observations of the 12 GHz methanol masers associated with this region. We also measure the trigonometric parallax and proper motion for G323.74–00.26 as $\pi = 0.364 \pm 0.009$ mas, $\mu_x = -3.239 \pm 0.025$ mas y^{−1} and $\mu_y = -3.976 \pm 0.039$ mas y^{−1}, which implies a distance of $d = 2.747 \pm 0.068$ kpc. These are the most accurate measurements of trigonometric parallax obtained for 6.7 GHz class II methanol masers to date. We confirm that G232.62+00.99 is in the Local arm and find that G323.74–00.26 is in the Scutum-Centaurus arm. We also investigate the structure and internal dynamics of both masers.

Keywords: astrometry - proper motions, parallaxes; masers - methanol; techniques - Very Long Baseline Interferometry

1. INTRODUCTION

Measuring the trigonometric parallax (hereafter ‘parallax’) and the proper motion of stars or star-forming regions that trace the motion of interstellar gas, is the best method to accurately determine the structure and kinematics of the Milky Way. Parallax measurements at radio frequencies have the advantage of not being obscured by dust, and can therefore probe much deeper into the disk of the Galaxy than those at optical frequencies.

Very Long Baseline Interferometry (VLBI) has been demonstrated to be able to achieve parallax accuracies

of ± 10 μ as and therefore measure objects at a distance of 10 kpc with 10% accuracy (Reid & Honma 2014). Thus far, this level of accuracy has been almost exclusively achieved at radio frequencies above 10 GHz and with homogeneous telescope arrays (e.g., the Very Long Baseline Array (VLBA)). At lower frequencies, uncompensated dispersive delays from the ionosphere can cause large systematic and direction-dependant errors (Rioja et al. 2017; Reid et al. 2017; Rioja & Dodson 2020).

MultiView (hereafter ‘direct MV’; Rioja et al. 2017), has been shown to give astrometric accuracies approaching values determined by the thermal noise. A new vari-

ation called inverse MultiView (iMV) has recently been developed that allows additional robust calibration of short-timescale quasi-random phases changes at the position of that target, for target-calibrator separations of up to 7° at 8.3 GHz (Hyland et al. 2022).

The Southern Hemisphere Parallax Interferometric Radio Astrometry Legacy Survey (S π RALS; Hyland 2021) is an extension of the Bar and Spiral Structure Legacy Survey (BeSSeL; Brunthaler et al. 2011; Reid et al. 2009b, 2014, 2019) and VLBI Exploration of Radio Astrometry (VERA; VERA Collaboration et al. 2020), with the aim to obtain information on the structure of the Milky Way for those regions exclusively visible from the southern hemisphere. S π RALS targets 6.7 GHz methanol masers (Menten 1991), which are known to exclusively trace high-mass star formation (Minier et al. 2001; Ellingsen 2007; Breen et al. 2013). At these relatively low frequencies, the iMV approach can greatly improve the calibration of the dispersive delays due to the ionosphere.

In this paper, we demonstrate the calibration capabilities of iMV by measuring $10\mu\text{s}$ -accurate parallaxes of two 6.7 GHz methanol masers. In Section 2 we describe target and calibrator selection, and observations. In Section 3 we outline all data reduction and analysis, including iMV calibration and parallax fitting. Section 4 presents the results and Section 5 includes a discussion of our findings.

2. METHODS

2.1. Source Selection and Observations

We selected two class II 6.7 GHz masers from the Methanol Multibeam Catalogue (MMB; Caswell et al. 2010, 2011; Green et al. 2012; Breen et al. 2015), which our pilot observations revealed to have compact emission in at least one $2\text{ kHz}/0.087\text{ km s}^{-1}$ velocity channel. The first was G232.62+00.99 (MacLeod et al. 1992), a maser associated with the HII region RCW 7 (Dubout-Crillon 1976). As this target is at a declination of -17° , it is visible from both the northern and southern hemispheres. Consequently, this maser region had an existing parallax measurement from the BeSSeL project (at 12 GHz; Reid et al. 2009a). This allows a direct comparison of parallaxes measured by the BeSSeL survey and S π RALS.

The second maser was G323.74–00.26 (MacLeod et al. 1992), one of the strongest 6.7 GHz methanol masers known, which has been exhibiting a peak flux density over 3000 Jy (while flares with flux density up to 5800 Jy have also been observed; Goedhart et al. 2004). This maser is at a declination of -56° and hence only visible to southern hemisphere instruments. There have been numerous studies of the 6.7 GHz methanol maser emis-

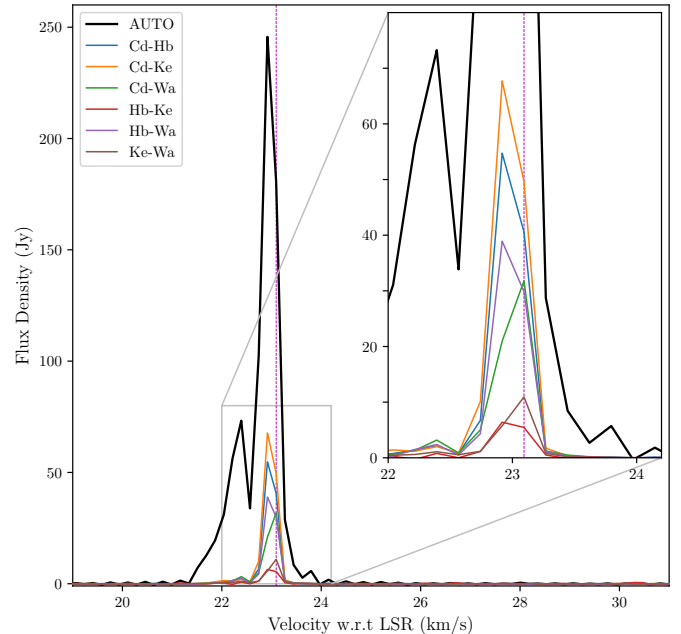


Figure 1. Auto- and cross-correlated spectra of G232.62+00.99 maser emission at epoch 6. Autocorrelated peak flux density (black line) is ~ 250 Jy and Ke-Wa (the longest baseline) cross-correlated peak flux density is 10 Jy. The reference feature at 23.08 km s^{-1} is indicated by the vertical magenta dashed line.

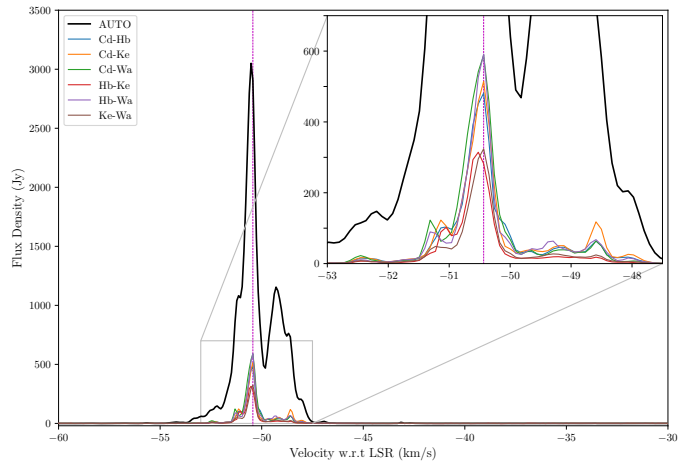


Figure 2. Auto- and cross-correlated spectra of G323.74–00.26 maser emission at epoch 4. Autocorrelated peak flux density is ~ 3500 Jy and Ke-Wa cross-correlated flux density (brown line) peaks as 300 Jy at velocity -50.52 km s^{-1} (indicated by the vertical-dashed magenta line).

sion associated with this region (Norris et al. 1993, 1998; Phillips et al. 1998; Walsh et al. 2002; Ellingsen 2007; Vlemmings et al. 2011).

The spectra of G232.62+00.99 and G323.74–00.26 as detected by our array are shown in Figure 1 and Figure 2, respectively.

Hyland et al. (2022) showed that iMV with calibrators up to $\approx 7^\circ$ separation from the target source can be successful at 8.3 GHz. At the lower frequency of 6.7 GHz, we chose calibrators separated by up to 5.5° . Allowing calibrators that are located up to this radius from a target provides many more bright and compact sources compared to the limitation that is usually applied for standard phase-referenced astrometric observations ($< 2^\circ$).

Therefore for both of the target masers, we selected calibrators that met the criteria (in order of priority):

- unresolved flux density > 100 mJy;
- within 5.5° separation;
- uniform directional sky sampling (with the target near the center).

For G232.62+00.99, we chose four calibrators separated by between 1 and 4° from the target (Table 1), originally from the catalog of Petrov et al. (2019). The fifth quasar at an angular separation of 5.3° (J0730–1141) was chosen as an electronic or “manual-phase” calibrator; however, its proximity to the target allowed incorporation into the iMV cycle.

For G323.74–00.26 we inferred the 6.7 GHz flux densities of calibrators from the available 8 GHz data (Petrov et al. 2019). Using the selection criteria above, we chose the 6 calibrators listed in Table 1. Note, there were no good¹ calibrators known within 2° of G323.74–00.26, and therefore standard phase referencing (PR) would have been difficult and likely to produce poor astrometric results.

The distribution of calibrators around the targets is shown in Figure 3, and Table 1 contains the calibrator positions and flux densities, listed in the order they were observed when nodding between the target and calibrator.

The structure of an individual observation session of nine hours was almost identical to that used by Hyland et al. (2022), with MultiView blocks bracketed by “geodetic-like” calibration blocks (Honma et al. 2007; Reid et al. 2009a; Reid & Honma 2014) and scans on bright compact calibrators. We observed seven epochs over a period of 1.5 years for G232.62+00.99 and seven epochs spanning 1 year for G323.74–00.26. The dates of

observations were chosen to sample near the extremes of the parallax oscillation in right ascension (R.A.) in order to optimize the accuracy to which the observations can measure the parallax. We refer to these maxima as “parallax seasons”.

2.2. Array, Frequency and Correlation

The array used for these observations is shown in Figure 4, comprising the University of Tasmania telescopes Ceduna 30m (Cd; McCulloch et al. 2005), Hobart 12m (Hb) and Katherine 12m (Ke; Lovell et al. 2013), and the Auckland University of Technology telescope Warkworth 30m (Wa; Woodburn et al. 2015). This array has a maximum baseline length of 4750 km.

We recorded data at 1024 Mbps in dual polarisation, Nyquist sampled at 2-bits per sample, over the frequency range 6580–6708 GHz. The Ceduna 30m and Warkworth 30m antennas recorded right and left (\mathcal{R}, \mathcal{L}) circular polarisations while Hobart 12m and Katherine 12m recorded horizontal and vertical (\mathcal{H}, \mathcal{V}) linear polarizations.

Baseband data were correlated using DiFX-2 (Deller et al. 2011) in two passes: all sources were correlated over the full recorded frequency range with 0.5 MHz frequency channels, and the iMV blocks were correlated in a 4 MHz “zoom” band approximately centered on the frequency of the maser emission. The zoom band data for G232.62+00.99 were correlated to give frequency channels of 4 kHz, corresponding to velocity channels of 0.174 km s^{-1} ; for G323.74–00.26 we used frequency channels of 2 kHz giving velocity channels of 0.087 km s^{-1} .

In order to create valid FITS files from our mixed polarisation (i.e., $\mathcal{HR}, \mathcal{VR}, \mathcal{HL}, \mathcal{VL}, \mathcal{RR}, \mathcal{LL}, \mathcal{RL}, \mathcal{LR}$) data (in *difx2fits*), we treated Hobart 12m and Katherine 12m \mathcal{H} as \mathcal{R} and \mathcal{V} as \mathcal{L} in our correlation. This approach was required as we were unsuccessful at converting the mixed polarisation products to a pure circular basis, owing to a lack of understanding of the complex apparent feed rotation characteristics of the Warkworth 30m (see Section 3.2). This would reduce the amplitudes of mixed polarization products by $\sqrt{2}$ (for an unpolarized source). Methanol masers at 6.7 GHz are known to exhibit low linear (typically 1.0–2.5%, max 17%) and circular polarization (typically 0.5–0.75%, max 6%; Surcis et al. 2022). The visibility amplitudes of the mixed products on both masers does not differ more than 20%, where we attribute most of this to a lack of exact amplitude and/or polarization calibration (e.g., Dodson 2008). In either case, we did not see any obvious adverse effects on our astrometric accuracy.

3. DATA REDUCTION AND ANALYSIS

¹ Those exhibiting a flux density greater than 100 mJy, with positions known to better than 0.3 mas and/or with little to no extended structure.

Table 1. Target maser and calibrator QSO *correlated* positions, angular separations and flux densities. QSOs are ordered in the sequence that they were observed. **Columns:** Target maser and calibrator QSO (1-2) name, right ascension and declination position (3-4), angular separation in right ascension and declination (5-6), total separation (7), and flux density (8).

Source Name		R.A.	Dec.	Separation			Flux
Target	Calibrator	(J2000)	(J2000)	$\Delta\alpha \cos \delta_T$	$\Delta\delta$	θ_{sep}	Density
Maser	QSOs	<i>h m s</i>	$^{\circ} \text{ } ' \text{ } ''$	($^{\circ}$)	($^{\circ}$)	($^{\circ}$)	(Jy)
G232.62+00.99		07 32 09.78	−16 58 12.80				$\sim 10^{\text{a}}$
	J0735−1735	07 35 45.812460	−17 35 48.50242	0.86	−0.62	1.06	0.10
	J0725−1904	07 25 50.165557	−19 04 19.07419	−1.51	−2.10	2.58	0.15
	J0729−1320	07 29 17.817692	−13 20 02.27125	−0.68	3.64	3.70	0.12
	J0748−1639	07 48 03.083813	−16 39 50.25355	3.80	0.31	3.81	0.30
	J0730−1141	07 30 19.112473	−11 41 12.60061	−0.44	5.28	5.30	3.18
G323.74−00.26		15 31 45.45	−56 30 50.10				$\sim 300^{\text{b}}$
	J1534−5351	15 34 20.660723	−53 51 13.42272	0.36	2.66	2.68	0.13 $^{\text{c}}$
	J1600−5811	16 00 12.377460	−58 11 02.96855	3.92	−1.67	4.18	0.32 $^{\text{c}}$
	J1524−5903	15 24 51.122912	−59 03 39.71702	−0.95	−2.55	2.71	0.06 $^{\text{c}}$
	J1512−5640	15 12 55.819395	−56 40 30.64300	−2.60	−0.16	2.60	0.20 $^{\text{c}}$
	J1515−5559	15 15 12.672909	−55 59 32.83823	−2.28	0.52	2.36	0.26 $^{\text{c}}$
	J1511−5203	15 11 08.926191	−52 03 47.25032	−2.84	4.45	5.37	0.05 $^{\text{c}}$

^aCorrelated flux density of +23.09 km s^{−1} channel at epoch 6 on Ke-Wa baseline (~ 4750 km)

^bCorrelated flux density of −50.52 km s^{−1} channel at epoch 4 on Ke-Wa baseline (~ 4750 km)

^cCatalogued unresolved flux density at 8.4 GHz.

3.1. Preliminary reduction

We calibrated correlated data in a similar manner to Hyland et al. (2022), with a few changes to account for dual-polarization/spectral line data, and that the targets may have significant positional changes over the year(s). Briefly, using *AZPS*/ParselTongue (Greisen 1990, 2003; Kettenis et al. 2006) the additional steps to calibrate the data were as follows:

1. Apparent feed rotation corrections were applied to the dual polarisation data with task CLCOR/PANG (see Section 3.2 for a detailed discussion of the complex correction needed for the Warkworth 30m antenna).
2. Source position shifts (to improve relative positions among the sources) were applied with task CLCAL/ANTP.
3. Tasks SETJY/CVEL were used to correct for the Earth’s (rotation and orbital) Doppler shift, ensuring that the maser spectra were aligned in frequency during and across epochs.
4. A maser channel was selected to be the phase reference and the task FRING was used to solve for the phase and rate on that single channel. The criteria for channel selection was maximum flux density on the long Katherine 12m–Warthworth 30m baseline.
5. The visibilities for the continuum sources were averaged in frequency using the task SPLIT, then the phases and rates from the maser reference channel were applied.
6. The calibrators were imaged using the IMAGR task. The position offset was determined for each calibrator and the weighted offsets of all calibrators were assumed to reflect a position error in the reference maser spot. The maser position corrections were measured for each observing season (x_T, y_T). Individual calibrator source offsets were used to refine their positions *relative* to the new maser position at one epoch. All position offsets were applied to each source in Step 2. *Important note:* The final calibrator positions were required to be consistent for all epochs.
7. The calibrators were averaged in frequency using the task SPLAT and the phase was measured with the CALIB task. The solutions were output and used for iMV fitting (described in Section 3.3)

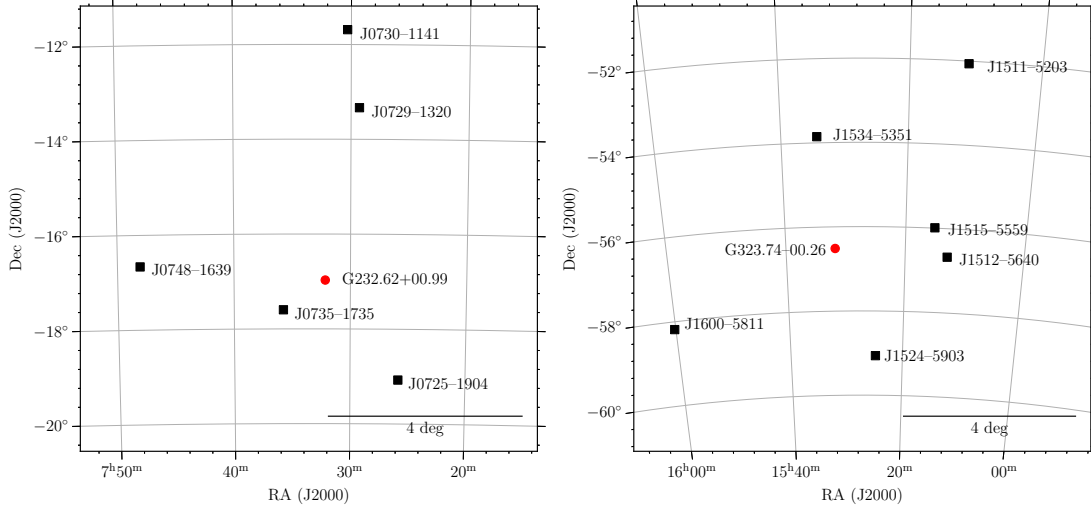


Figure 3. Sky distributions of target masers (red dot) and calibrators (black squares). **Left:** Target maser G232.62+00.99 with 5 calibrator QSOs. The smallest calibrator separation is 1.06° (J0735–1735) and the largest is 5.30° (J1730–1141). **Right:** Target maser G323.740–0.263 with 6 calibrator QSOs. Smallest calibrator separation is 2.36° (J1515–5559) and largest is 5.37° (J1511–5203).

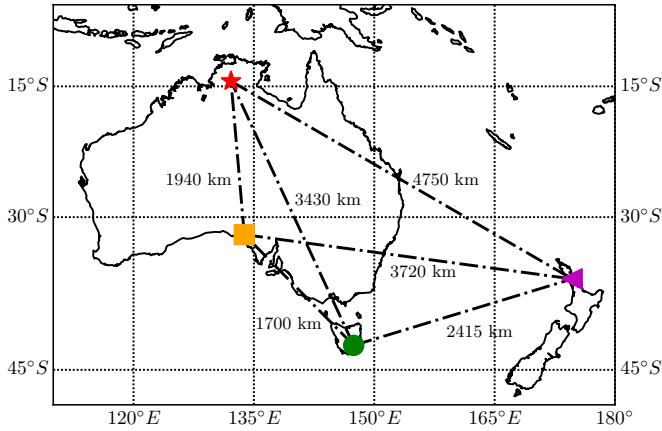


Figure 4. VLBI array used for these observations, with the University of Tasmania telescopes Ceduna 30m (orange square), Hobart 12m (green circle), Katherine 12m (red star) and Auckland University of Technology telescope Warkworth 30m (purple triangle). Baselines are indicated with dash-dotted lines and baseline lengths are given next to corresponding baselines.

3.2. Warkworth 30m Apparent Feed Rotation Correction

The Warkworth 30m antenna is a Nasmyth wheel-on-track antenna with a beam waveguide design (Petrov et al. 2015). The physical feed does not rotate when the antenna moves and a system of four mirrors directs the beam into the receiver; i.e., a Beam Wave-Guide system, which is not uncommon for converted telecom antennas (Warkworth NZ, Yamaguchi JP, Nkutunse GH, etc.). At the time of analysis, the standard *AIPS* task CLCOR/PANG did not include corrections for this type

of focus. In order to combine the dual polarisation data we needed to correct for the phase introduced as the antenna moves in azimuth and elevation.

We found the phase correction, φ , that accounts for the apparent feed rotation is:

$$\varphi = -q - \mathcal{A} + \mathcal{E} \quad (1)$$

where q is the parallactic angle, \mathcal{A} is the azimuth angle (measured North through East), and \mathcal{E} is the elevation angle. Subtracting φ from the RCP signal (\mathcal{R}) and adding it to the LCP signal (\mathcal{L}) phase corrects the visibility data for the apparent feed rotation, allowing the \mathcal{R} and \mathcal{L} data to be averaged before fringe fitting on the maser and increasing the S/N by a factor of $\sqrt{2}$. The feed correction has subsequently been added to the CLCOR task and the technical details are described in Dodson & Rioja (2022).

3.3. iMV Calibration

Given the existence of occasional phase wraps in the 8.3 GHz experiments described by Hyland et al. (2022), we expected a similar or greater number to be present at 6.7 GHz. The residual path delay, $\Delta\tau$, for a dispersive medium like the ionosphere scales with frequency, ν , as ν^{-2} . Interferometer phase, ϕ , is given by $\phi = \Delta\tau \nu$, and thus the effect on phase scales as ν^{-1} . Therefore, scaling from 8.3 GHz to 6.7 GHz should lead to a 20% increase in phase shifts (assuming the same value for the residual total electron content TEC). This implies there is likely to be an increased number of phase wraps in our 6.7 GHz data compared to those seen by Hyland et al. (2022).

In order to unwrap the phases, we took the minimum difference of phase between consecutive scans on the same calibrator when adding trial values of 360° , 0° , and -360° . Additionally, all phases were minimized relative to a common time at the center of the track, where the delay errors due to residual tropospheric and ionospheric errors are expected to be at a minimum.

Once unwrapped, the phase data on each scan was fit with the least squares method to a model for a 2D plane (see Equation 5 from Hyland et al. (2022)) and the interpolated phase at the origin was subtracted from the maser visibility data using the task CLCAL.

The maser reference channel was then imaged using the *AIPS* task IMAGR, and the brightness distribution was fitted with a Gaussian model using the task JMFIT in order to measure the astrometric offsets (x_m, y_m) from the original phase center in Table 2.

3.4. Position shifting and parallax fitting

In order to minimize phase wraps (see the previous section), the (moving) maser position was updated at each observing season. In order to put the measured positions back into a stationary reference frame, one must undo these shifts before fitting the parallax and proper motion. To achieve this, we first chose a reference position shift from the correlated position: \tilde{x}_T, \tilde{y}_T . We then calculated the offset from this reference position at each epoch (i.e., $x_T - \tilde{x}_T$) and added it to the measured maser offset from the synthesized images (x_m, y_m). This gave the total offset from the reference position over time ($x_{\text{tot}}, y_{\text{tot}}$). These values are given in Table 2.

We fit the ($x_{\text{tot}}, y_{\text{tot}}$) data using the model of Equation 2 in the Appendix with variance-weighted least-squares to determine the parallax (π), and the proper motions (μ_x, μ_y). Since astrometric uncertainty is usually dominated by systematic error, whose magnitude is not known *a priori*, we added “error floors” to the x and y data in quadrature. We independently varied these error floors to achieve a chi-squared per degree of freedom of unity for each coordinate. This approach is widely used in maser astrometry and is considered the most reliable method for estimating the uncertainties in π, μ_x, μ_y (Reid et al. 2009a). The models as fit to the astrometric data for each target are shown in Figure 5 and Figure 6.

4. RESULTS

Using iMV, we measure the parallax and proper motion of the 6.7 GHz emission in G232.62+00.99 to be $\pi = 0.610 \pm 0.011$ mas, $\mu_x = -2.266 \pm 0.021$ mas y^{-1} , and $\mu_y = 2.249 \pm 0.049$ mas y^{-1} . This yields a distance of $d = 1.639 \pm 0.030$ kpc (i.e., parallax inversion $d = 1/\pi$ with symmetric errors $\sigma_d = \sigma_\pi/\pi^2$). For

G323.74–00.26, we measure a parallax of $\pi = 0.364 \pm 0.009$ mas and proper motion of $\mu_x = -3.239 \pm 0.025$ and $\mu_y = -3.976 \pm 0.039$ mas y^{-1} , yielding a distance of $d = 2.747 \pm 0.068$ kpc.

In order to evaluate the astrometric improvement of iMV compared to standard (inverse) phase referencing using a single-calibrator, we also estimated parallaxes relative to each quasar in each cluster. We find that the parallaxes based on individual calibrators in the G232.62+00.99 cluster range from 0.433 to 0.636 mas and in the G323.74–00.26 cluster range from 0.294 to 0.484 mas. These results are consistent with systematic parallax shifts of magnitude ~ 0.05 mas per degree of calibrator angular offset found by Reid et al. (2017). All of the parallax and proper motion results are tabulated in Table 3.

5. DISCUSSION

5.1. G232.62+00.99

The parallax and proper motion of the 12 GHz methanol emission in G232.62+1.0 were measured with the VLBA between October 2005 and March 2007 to be $\pi = 0.596 \pm 0.035$ mas, $\mu_x = -2.17 \pm 0.06$ mas y^{-1} , $\mu_y = 2.09 \pm 0.46$ mas y^{-1} (Reid et al. 2009a). Compared to this previous measurement, the parallax and proper motions of the 6.7 GHz methanol and 12 GHz methanol masers agree within the quoted uncertainties, with the obvious difference being that the new estimate is 3-times more accurate for π and μ_x and an order of magnitude more accurate for μ_y .

It should be noted that the previous measurement was subject to issues that limited the performance of the VLBA: namely the source was observed at very low elevations and, the 12 GHz emission was resolved and only the inner five VLBA antennas were used, limiting the maximum baseline length to 1500 km (compared to the maximum baseline we use of 4750 km). Accounting for the latter by simply dividing the previous parallax measurement uncertainty by ~ 3 reduces it to $\pm 12 \mu\text{as}$. This indicates that we were able to successfully calibrate the delays (primarily the ionosphere) at 6.7 GHz to at least the same levels as could be achieved at 12 GHz, if not better.

The previous southern hemisphere 6.7 GHz methanol maser parallaxes were measured by Krishnan et al. (2015, 2017) on the Long Baseline Array – another southern hemisphere VLBI array that has common telescopes with the array that we used. These measurements were plagued by uncompensated dispersive delays, leading to parallaxes with accuracy between 50 – 110 μas . Compared to the $\sim 10 \mu\text{as}$ parallaxes we have

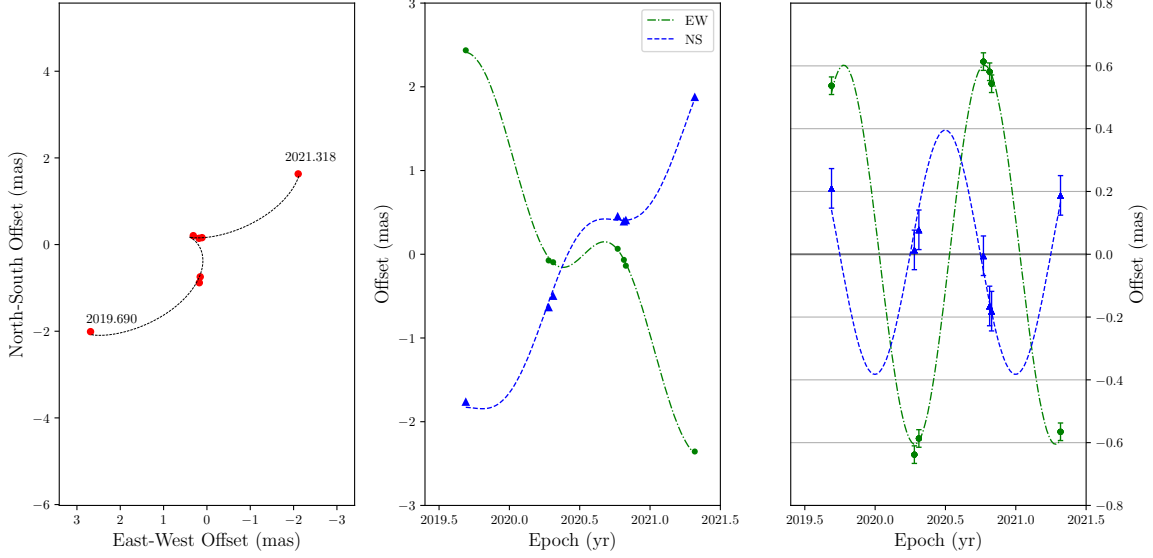


Figure 5. Parallax and proper motion modelling of G232.62+00.99 velocity channel $v = 23.08 \text{ km s}^{-1}$. **Left:** Total sky position change over the full observation period. **Middle:** Decomposition of sky motion into East-West (green dot-dashed) and North-South (blue dashed) motion over time. **Right:** Proper-motion subtracted sky motion over time. Error bars include 1σ error floors for each coordinate of $28\mu\text{as}$ and $62\mu\text{as}$ for the EW and NS directions respectively.

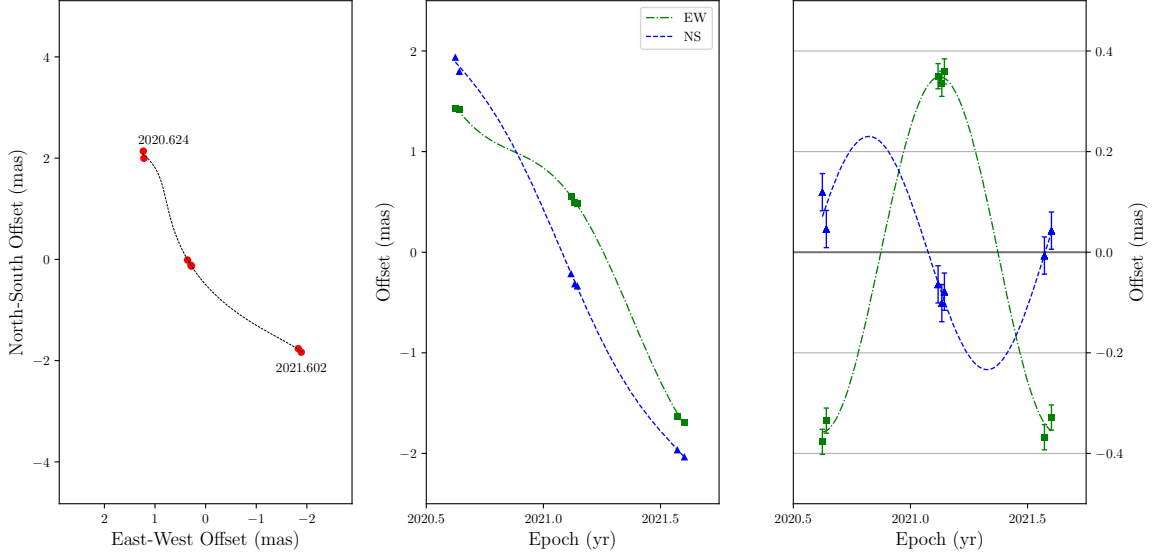


Figure 6. Parallax and proper motion modelling of G323.74-00.26 velocity channel $v = -50.52 \text{ km s}^{-1}$. **Left:** Total sky position change over the full observation period. **Middle:** Decomposition of sky motion into East-West (green dot-dashed) and North-South (blue dashed) motion over time. **Right:** Parallax motion (i.e., proper-motion subtracted) over time. Error bars show independent 1σ error floors for each direction as $25\mu\text{as}$ and $39\mu\text{as}$ for the EW and NS directions respectively.

measured, we can see there has been a marked improvement owing to MV techniques.

The methanol maser emission towards G232.62+00.99 can be grouped into four regions, with the northernmost being the brightest. The regions are distributed in a slightly arched or linear arrangement, and have a velocity gradient running South-East to North-West. The positions and internal motions relative to the reference

feature are shown in Figure 7. The internal motions of the region relative to the reference maser feature are small, only $\leq 0.33 \text{ mas/yr}$ or 2.6 km s^{-1} at the measured distance. This suggests that the internal motion of the reference feature is also small and that the measured proper motion of that feature is representative of the region as a whole. We have inflated the error in the region proper motion to 0.33 mas/yr (Table 3) to ac-

Table 2. Epochs of VLBI observations and astrometric positions.

Target	Epoch	Date	Target Shift		w.r.t Ref. pos		Meas. Offset		Total Offset	
			x_T	y_T	$x_T - \tilde{x}_T$	$y_T - \tilde{y}_T$	x_m	y_m	x_{tot}	y_{tot}
			(mas)	(mas)	(mas)	(mas)	(mas)	(mas)	(mas)	(mas)
G232.62+00.99	1	2019 Sep 09	20.82	242.083	2.7	-2.2	-0.028	0.177	2.692	-2.023
	2	2020 Apr 12	18.42	243.583	0.3	-0.7	-0.146	-0.203	0.154	-0.903
	3	2020 Apr 24	18.42	243.583	0.3	-0.7	-0.212	-0.263	0.088	-0.963
	4	2020 Oct 09	18.22	244.383	0.1	0.1	0.208	0.110	0.308	0.210
	5	2020 Oct 25	18.22	244.383	0.1	0.1	-0.009	0.093	0.091	0.193
	6	2020 Oct 30	18.22	244.383	0.1	0.1	-0.043	0.063	0.057	0.163
	7	2021 Apr 26	16.22	245.883	-1.9	1.6	-0.203	-0.017	-2.103	1.583
	<i>Ref. pos</i> (\tilde{x}_T, \tilde{y}_T):		18.12	244.283						
G323.74-00.26	1	2020 Aug 15	-187.1	-177.7	1.5	1.9	-0.268	0.239	1.232	2.139
	2	2020 Aug 21	-187.1	-177.7	1.5	1.9	-0.281	0.098	1.219	1.998
	3	2021 Feb 12	-188.3	-179.6	0.3	0.0	0.058	0.012	0.358	-0.012
	4	2021 Feb 18	-188.3	-179.6	0.3	0.0	-0.009	-0.143	0.291	-0.143
	5	2021 Feb 22	-188.3	-179.6	0.3	0.0	-0.020	-0.114	0.280	-0.114
	6	2021 Jul 28	-190.4	-181.4	-1.8	-1.8	-0.031	0.037	-1.831	-1.763
	7	2021 Aug 08	-190.4	-181.4	-1.8	-1.8	-0.089	-0.033	-1.889	-1.833
	<i>Ref. pos</i> (\tilde{x}_T, \tilde{y}_T):		-188.6	-179.6						

count for this. The weakest consistently-detected maser spot was 2 Jy, and the measured maser spot distribution is consistent with that reported by Fujisawa et al. (2014).

G232.62+00.99 well-matches the (l, b) coordinates of the Local arm as traced by Reid et al. (2019). The centroid velocity of the associated 6.7 GHz masers is near 23 km s^{-1} , which compares reasonably with 17 km s^{-1} fitted to Local arm sources nearby in angle.

The center of the Local arm at longitude 232° is at a distance of 0.83 kpc, and the estimated Gaussian 1σ width of an arm at a Galactocentric radius of 9 kpc is 0.4 kpc (Reid et al. 2019). At our measured distance of 1.64 kpc, this places G232.62+00.99 at 0.81 kpc (or about 2σ) from the arm center. Since this source is at one end (at Galactic azimuth -8°) of sources with measured parallaxes used to trace the Local arm, it could be that the pitch angle fitted over that azimuth range extending to the other end (azimuth $+34^\circ$) should be increased slightly. Interestingly, however, there is a “bridge” of gas seen in HI starting at $(l, V_{lsr}) = (232^\circ, 20 \text{ km s}^{-1})$ and connecting to the Perseus arm at $(242^\circ, 70 \text{ km s}^{-1})$ (see Fig. 12 of Reid et al. 2016). Possibly, G232.62+00.99 is associated with this bridge.

5.2. G323.74-00.26

G323.74-00.26 is clearly associated with the Scutum-Centaurus spiral arm, since its (l, b, V_{lsr}) coordinates of $(323^\circ 74', -0^\circ 26', -50 \text{ km s}^{-1})$ compare very well with the arm model of $(323^\circ, -0^\circ 01', -53 \text{ km s}^{-1})$ of Reid et al. (2019). That model places the center of the arm at this longitude at a distance of 3.2 kpc, which is about 0.45 kpc more distant than our parallax. At a Galactocentric radius of 6.1 kpc the arm width estimate of Reid et al. (2019) is 0.26 kpc, placing this source 1.7σ from the center. However, given that at present very few southern sources have accurate parallax measurements, this is not surprising, since the precise location of the Centaurus arm segment might be fairly uncertain at this time.

The G323.74-00.26 maser emissions arise from quite a large number of spots. Figure 8 shows the positions of bright spots and their apparent motions over time. We have subtracted the average motion of $\mu_{x_{int}} = 0.00 \pm 0.02$ and $\mu_{y_{int}} = -0.198 \pm 0.012 \text{ mas y}^{-1}$ in the R.A. and declination directions respectively. If the distribution of measured spot motion is near-isotropic, this average will reflect the internal motion of the reference feature. Therefore we also subtracted this motion from the measured proper motion of the reference feature measured with respect to the quasars (Table 3) to obtain an estimate of the absolute motion of the region giving

Table 3. Trigonometric parallaxes and proper motions determined from iPR from the target maser, and iMV.

Source	θ_{sep}	π	μ_x	μ_y	Num.	
Target	Background	($^{\circ}$)	(mas)	(mas y $^{-1}$)	Epochs	
G232.62+00.99	J0735–1735	1.06	0.523 ± 0.055	-2.367 ± 0.100	2.353 ± 0.100	6
	J0725–1904	2.58	0.634 ± 0.053	-2.221 ± 0.098	2.155 ± 0.204	7
	J0729–1320	3.70	0.636 ± 0.048	-2.175 ± 0.085	2.533 ± 0.128	6
	J0748–1639	3.81	0.433 ± 0.024	-2.252 ± 0.043	2.958 ± 0.142	6
	J0730–1141 ^a	5.30	-	-	-	-
	<i>iMV w/ all</i>		0.610 ± 0.011	-2.266 ± 0.021	2.249 ± 0.049	7
	<i>inc. int. mot.</i>			-2.266 ± 0.330	2.249 ± 0.330	
G323.74–00.26	J1515–5559	2.36	0.359 ± 0.027	-3.25 ± 0.08	-4.01 ± 0.10	7
	J1512–5640	2.60	0.374 ± 0.032	-3.23 ± 0.09	-3.83 ± 0.25	7
	J1534–5351	2.68	0.437 ± 0.028	-3.20 ± 0.08	-3.89 ± 0.15	7
	J1524–5903 ^b	2.71	-	-	-	3
	J1600–5811	4.18	0.294 ± 0.051	-3.06 ± 0.14	-3.72 ± 0.19	7
	J1511–5203	5.37	0.484 ± 0.059	-3.57 ± 0.18	-3.71 ± 0.25	6
	<i>iMV w/ all</i>		0.364 ± 0.009	-3.239 ± 0.025	-3.976 ± 0.039	7
	<i>inc. int. mot.</i>			-3.239 ± 0.400	-4.174 ± 0.400	

NOTE—iMV results attained using data from all QSOs. *Inc. int. mot.* abbreviates including internal motions.

^aiPR from G232.62+00.99 to QSO J0730–1141 did not produce coherent synthesized images at any epoch.

^biPR from G323.74–00.26 to QSO J1524–5903 only produced coherent at three out of seven epochs.

$\mu_{x_{\text{tot}}} = -3.2 \pm 0.4$ and $\mu_{y_{\text{tot}}} = -4.2 \pm 0.4$ mas y $^{-1}$. Here we have added an additional uncertainty of 0.4 mas y $^{-1}$ in quadrature (equivalent to 5 km s $^{-1}$ at the measured distance) to account for the likelihood that the spots do not have an isotropic velocity distribution. There does not seem to be significant evidence in favor of an edge-on disk structure as has been suggested for this methanol maser (e.g., Phillips et al. 1998), and the structure and internal motions instead suggest that the maser spot distribution may be part of a bow shock.

The peculiar (non-circular) motion of G323.74–00.26 about the Galactic Center of mass can be calculated from its measured 6-dimensional phase-space values. Adopting a $V_{\text{lsr}} = 50.5 \pm 5.0$ km s $^{-1}$ and the rotation curve of Reid et al. (2019), we find $(U_p, V_p, W_p) = (-5, -1, -8)$ km s $^{-1}$, where U_p is toward the Galactic center at the position of the source, V_p is in the direction of Galactic rotation, and W_p is toward the North Galactic Pole. Uncertainties from measurement error are ± 5 km s $^{-1}$ in each coordinate, so G323.74–00.26 has a very small peculiar motion as is typical for a young high-mass star.

5.3. Inverse MultiView

Comparing the parallax and proper motion results from iMV with a group of calibrators to standard (inverse) phase referencing with a single calibrator (Table 3), we find that iMV is at least a factor of two better in accuracy. In Hyland et al. (2022), per-epoch positional uncertainties of $\pm 20 \mu\text{as}$ were achieved at 8.3 GHz for calibrator separations $< 7^\circ$ in both NS and EW directions. Here we report per-epoch positional uncertainties (determined from the error floor values) of $\approx 26 \mu\text{as}$ in the EW direction and $\approx 50 \mu\text{as}$ in the NS direction.

Figure 9 shows the difference between the iMV and iPR parallaxes as a function of total angular separation for both targets. Under the assumption that the iMV parallax is the true parallax, this plot shows the systematic error of iPR parallaxes vs. target-calibrator separation. The behavior of the G323.74–00.26 iPR parallaxes is exactly as expected, where the error increases with target-calibrator separation. For G232.62+00.99 there is a larger spread and no clear trend. In both cases, all parallaxes based on different quasars have much more uncertain parallax fits.

Comparisons between the relative performance of iMV and iPR is inequitable because the experiments were specifically tailored for iMV. However, in comparison

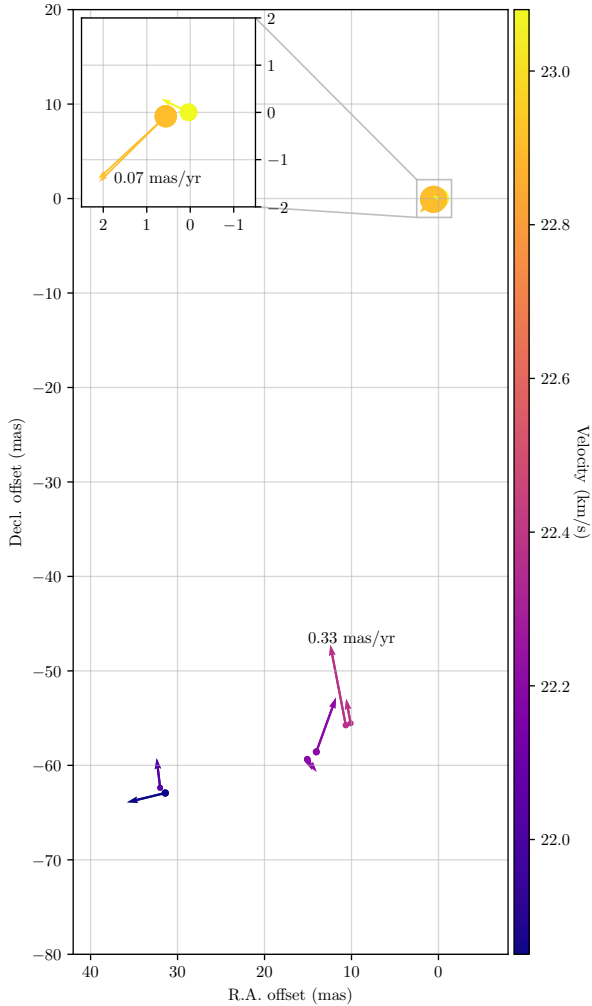


Figure 7. Map of methanol maser spots in G232.62+00.99 and their proper motions relative to the reference spot at (0,0). Features shown were detected in ≥ 5 epochs. **Top left:** Zoomed-in section around (0,0) shows the main emission region is a blended-double.

with past 6.7 GHz parallax experiments (e.g., Krishnan et al. 2015, 2017; Reid et al. 2017) is it clear that our additional calibration steps have reduced astrometric uncertainty, and/or removed possible systematic errors that may have been introduced in the parallax fit.

It is important to note that for at least one quasar per maser, an iPR parallax was unable to be determined. Once for the most distant calibrator (J1730–141), and the other for an intermediate distance calibrator (J1524–5903, Table 3). In both cases, the quasar in question was not visible in synthesized images at a number of epochs, presumably due to the uncalibrated delay slopes and perhaps additionally in the case of J1524, low flux density.

For this reason, we stress the use of numerous compact and strong calibrators with good positions, which

allow the original maser position to be updated despite the presence of uncalibrated delays (i.e., in step 6 of preliminary reduction). It appears that five calibrators are the ideal number, allowing a balance between spatial and temporal sampling, while four calibrators should be considered the bare minimum. For specific linear arrangements of the target and calibrators, fewer may be acceptable.

6. CONCLUDING REMARKS

We have used inverse MultiView to measure the parallax and proper motion of two 6.7 GHz class II methanol masers, with results approaching the highest accuracy ever achieved at this frequency.

As part of the S π RALS project, we will continue to measure the parallaxes and proper motions for southern hemisphere 6.7 GHz class II methanol masers to fill in the 4th quadrant to better trace the spiral arms of the Milky Way. Based on the current array capabilities and preliminary surveys of compact maser emission on VLBI baselines (Hyland 2021), we estimate there are at least 20 masers that are bright and compact enough to measure parallax with iMV in the current iteration of S π RALS. We also aim to explore the application of direct MV (Rioja et al. 2017) to measure parallaxes and proper motions to the weaker methanol masers inappropriate for iMV, which may double the number of possible targets.

DATA AND CODE AVAILABILITY

The data underlying this article will be shared on reasonable request to the corresponding author. The scripts and programs used for data reduction and calibration are available at <https://github.com/lucasjord/spirals/script>. Data behind Figures 1, 2, 7 and 8 are available at https://github.com/lucasjord/spirals/imultiview_p2.

ACKNOWLEDGEMENTS

This research was supported by the Australian Research Council (ARC) Discovery Grant DP180101061. We want to thank Mr Brett Reid and Mrs Bev Benson for maintaining and organizing the University of Tasmania radio telescopes. We acknowledge the Jawoyn, Paredarmerne, and Wirangu peoples as the traditional owners of the land siting the Katherine, Hobart, and Ceduna telescopes respectively. The Warkworth 30m radio telescope is funded and operated by the Auckland University of Technology; we would like to thank Mr. Lewis Woodburn for the maintenance and management of this facility to enable its involvement in this project. This research has made use of NASAs

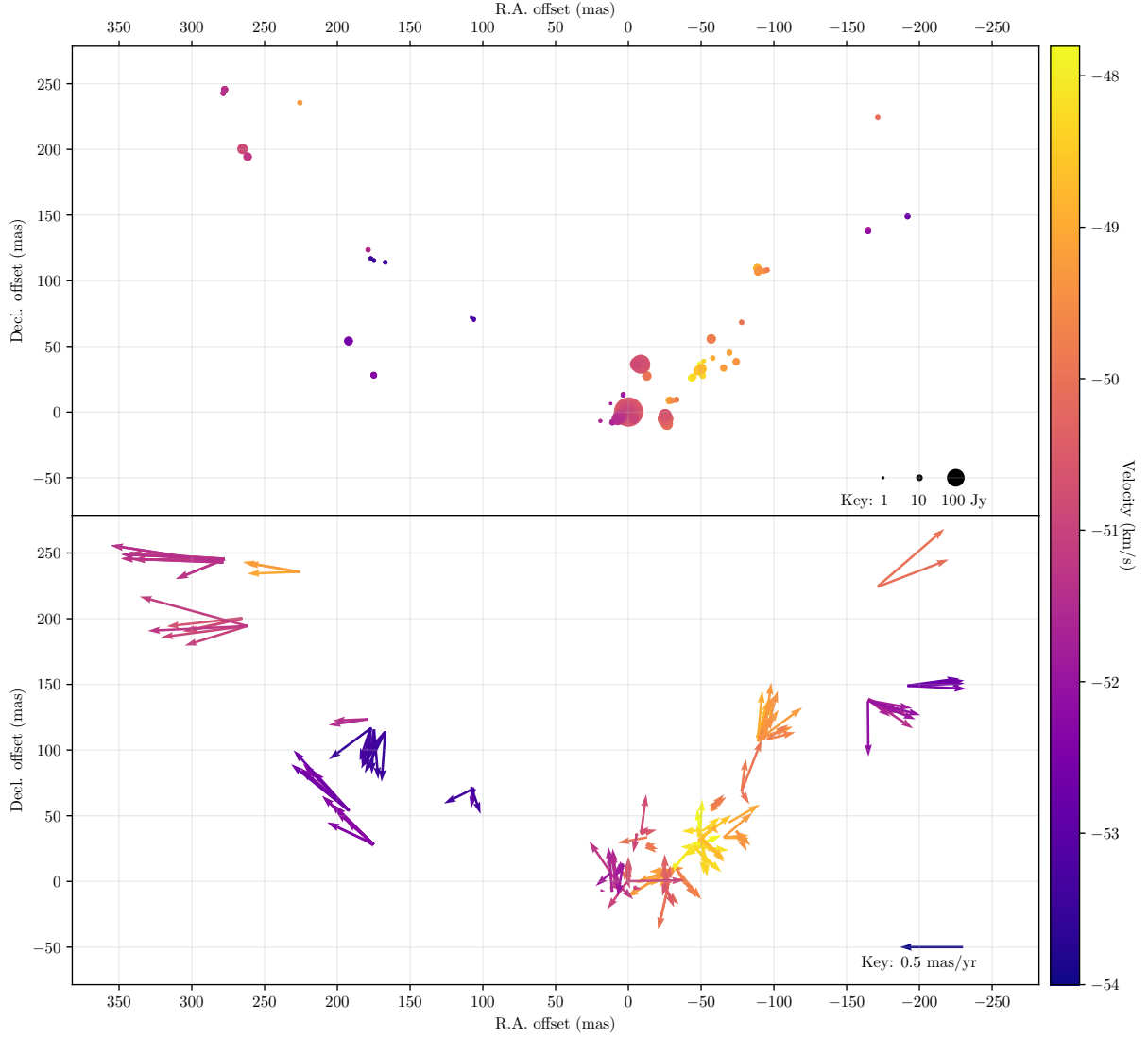


Figure 8. Map and dynamics of maser spots in G323.74–00.26. **Top:** Positions and flux densities of maser spots. **Bottom:** Internal motions of maser spots. Features shown were detected in ≥ 5 epochs.

Astrophysics Data System Abstract Service. This research made use of [MaserDB.net](https://maserdb.net), an online database of astrophysical masers (Ladeyschikov et al. 2019). This research made use of Astropy, a community-developed core Python package for Astronomy (Astropy Collaboration et al. 2013, 2018).

APPENDIX

The model used to predict the position of the target (x, y) at any given time (t) relative to some reference time (t_0) due to parallax (π) and proper motion (μ_x, μ_y)

is as follows:

$$\begin{aligned} x &= \pi(Y \cos \alpha - X \sin \alpha) + \mu_x(t - t_0) \\ y &= \pi(Z \cos \delta - X \cos \alpha \sin \delta \\ &\quad - Y \sin \alpha \sin \delta) + \mu_y(t - t_0) \end{aligned} \quad (2)$$

where α and δ are the R.A. and Dec. of the target, and X, Y, Z represent the Earth’s position relative to the Sun at epoch t (as determined by the NOVAS subroutines; Kaplan et al. (1989)). Since the NOVAS routines request t in MJD, the μ values are returned in mas d^{-1} .

REFERENCES

Astropy Collaboration, Robitaille, T. P., Tollerud, E. J., et al. 2013, *A&A*, 558, A33

Astropy Collaboration, Price-Whelan, A. M., Sipőcz, B. M., et al. 2018, *AJ*, 156, 123

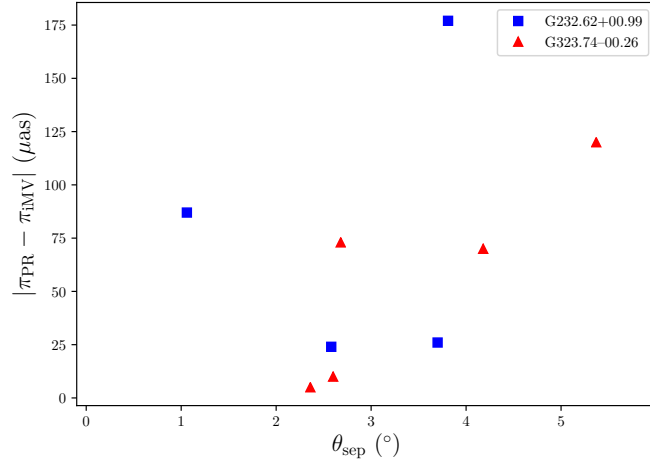


Figure 9. Absolute difference between parallaxes determined with iMV and iPR for each maser.

- Breen, S. L., Ellingsen, S. P., Contreras, Y., et al. 2013, *MNRAS*, **435**, 524
- Breen, S. L., Fuller, G. A., Caswell, J. L., et al. 2015, *MNRAS*, **450**, 4109
- Brunthaler, A., Reid, M. J., Menten, K. M., et al. 2011, *Astronomische Nachrichten*, **332**, 461
- Caswell, J. L., Fuller, G. A., Green, J. A., et al. 2010, *MNRAS*, **404**, 1029
- . 2011, *MNRAS*, **417**, 1964
- Deller, A. T., Briskeen, W. F., Phillips, C. J., et al. 2011, *PASP*, **123**, 275
- Dodson, R. 2008, *A&A*, **480**, 767
- Dodson, R., & Rioja, M. J. 2022, in eLBA memo 14
- Dubout-Crillon, R. 1976, *A&AS*, **25**, 25
- Ellingsen, S. P. 2007, *MNRAS*, **377**, 571
- Fujisawa, K., Sugiyama, K., Motogi, K., et al. 2014, *PASJ*, **66**, 31
- Goedhart, S., Gaylard, M. J., & van der Walt, D. J. 2004, *MNRAS*, **355**, 553
- Green, J. A., Caswell, J. L., Fuller, G. A., et al. 2012, *MNRAS*, **420**, 3108
- Greisen, E. W. 1990, in *Acquisition, Processing and Archiving of Astronomical Images*, 125
- Greisen, E. W. 2003, in *Astrophysics and Space Science Library*, Vol. 285, *Information Handling in Astronomy - Historical Vistas*, ed. A. Heck, 109
- Honma, M., Bushimata, T., Choi, Y. K., et al. 2007, *PASJ*, **59**, 889
- Hyland, L. J. 2021, PhD thesis, School of Natural Sciences
- Hyland, L. J., Reid, M. J., Ellingsen, S. P., et al. 2022, *ApJ*, **932**, 52
- Kaplan, G. H., Hughes, J. A., Seidelmann, P. K., Smith, C. A., & Yallop, B. D. 1989, *AJ*, **97**, 1197
- Kettenis, M., van Langevelde, H. J., Reynolds, C., & Cotton, B. 2006, in *Astronomical Society of the Pacific Conference Series*, Vol. 351, *Astronomical Data Analysis Software and Systems XV*, ed. C. Gabriel, C. Arviset, D. Ponz, & S. Enrique, 497
- Krishnan, V., Ellingsen, S. P., Reid, M. J., et al. 2017, *MNRAS*, **465**, 1095
- . 2015, *ApJ*, **805**, 129
- Ladeyschikov, D. A., Bayandina, O. S., & Sobolev, A. M. 2019, *AJ*, **158**, 233
- Lovell, J. E. J., McCallum, J. N., Reid, P. B., et al. 2013, *Journal of Geodesy*, **87**, 527
- MacLeod, G. C., Gaylard, M. J., & Nicolson, G. D. 1992, *MNRAS*, **254**, 1P
- McCulloch, P. M., Ellingsen, S. P., Jauncey, D. L., et al. 2005, *AJ*, **129**, 2034
- Menten, K. M. 1991, *ApJL*, **380**, L75
- Minier, V., Conway, J. E., & Booth, R. S. 2001, *A&A*, **369**, 278
- Norris, R. P., Whiteoak, J. B., Caswell, J. L., Wieringa, M. H., & Gough, R. G. 1993, *ApJ*, **412**, 222
- Norris, R. P., Byleveld, S. E., Diamond, P. J., et al. 1998, *ApJ*, **508**, 275
- Petrov, L., de Witt, A., Sadler, E. M., Phillips, C., & Horiuchi, S. 2019, *MNRAS*, **485**, 88
- Petrov, L., Natusch, T., Weston, S., et al. 2015, *PASP*, **127**, 516
- Phillips, C. J., Norris, R. P., Ellingsen, S. P., & McCulloch, P. M. 1998, *MNRAS*, **300**, 1131
- Reid, M. J., Dame, T. M., Menten, K. M., & Brunthaler, A. 2016, *ApJ*, **823**, 77
- Reid, M. J., & Honma, M. 2014, *ARA&A*, **52**, 339
- Reid, M. J., Menten, K. M., Brunthaler, A., et al. 2009a, *ApJ*, **693**, 397

- Reid, M. J., Menten, K. M., Zheng, X. W., et al. 2009b, [ApJ](#), **700**, 137
- Reid, M. J., Menten, K. M., Brunthaler, A., et al. 2014, [ApJ](#), **783**, 130
- Reid, M. J., Brunthaler, A., Menten, K. M., et al. 2017, [AJ](#), **154**, 63
- Reid, M. J., Menten, K. M., Brunthaler, A., et al. 2019, [ApJ](#), **885**, 131
- Rioja, M. J., & Dodson, R. 2020, [A&A Rv](#), **28**, 6
- Rioja, M. J., Dodson, R., Orosz, G., Imai, H., & Frey, S. 2017, [AJ](#), **153**, 105
- Surcis, G., Vlemmings, W. H. T., van Langevelde, H. J., Hutawarakorn Kramer, B., & Bartkiewicz, A. 2022, [A&A](#), **658**, A78
- VERA Collaboration, Hirota, T., Nagayama, T., et al. 2020, [PASJ](#), [arXiv:2002.03089 \[astro-ph.GA\]](#)
- Vlemmings, W. H. T., Torres, R. M., & Dodson, R. 2011, [A&A](#), **529**, A95
- Walsh, A. J., Lee, J. K., & Burton, M. G. 2002, [MNRAS](#), **329**, 475
- Woodburn, L., Natusch, T., Weston, S., et al. 2015, [PASA](#), **32**, 17